Eur. Phys. J. D **30**, 379–392 (2004)
DOI: 10.1140/epjd/e2004-00102-7

THE EUROPEAN PHYSICAL JOURNAL D

Predicting intense-field photoionization of atoms and molecules from their linear photoabsorption spectra in the ionization continuum

C.J.G.J. Uiterwaal[1], C.R. Gebhardt[2], H. Schröder[2,a], and K.-L. Kompa[2]

[1] Department of Physics and Astronomy, The University of Nebraska - Lincoln, Behlen Lab - City Campus, Lincoln, NE 68588-0111, USA
[2] Max-Planck-Institut für Quantenoptik, Hans-Kopfermann-Straße 1, 85748 Garching, Germany

Received 8 October 2003 / Received in final form 20 January 2004
Published online 17 August 2004 –

Abstract. We report a new approach to intense-field photoionization that is based on the ad hoc assumption that m photons of energy $E_{\rm ph}$ arriving within a typical electronic response time are effectively equivalent to a single photon of energy $mE_{\rm ph}$. The heuristic model contains no adjustable parameters and unifies apparent multiphoton and field aspects. Moreover, nonsequential, suppressed and above-threshold ionization phenomena become readily understandable. Predicted ionization intensities are in satisfactory agreement with available experimental data ranging from C_6H_6 to Ne^{3+}, from femtosecond to nanosecond laser pulses, and from ultraviolet to infrared laser radiation.

PACS. 32.80.Rm Multiphoton ionization and excitation to highly excited states (e.g., Rydberg states) – 32.80.Wr Other multiphoton processes – 42.50.Hz Strong-field excitation of optical transitions in quantum systems; multiphoton processes; dynamic Stark shift

1 Introduction

Present concepts to understand nonresonant high-intensity laser ionization of atoms and molecules implicate electron tunneling enabled by the laser's instantaneous electric field as the fundamental mechanism [1,2]. Several models have been developed to describe intense-field ionization, among which the Ammosov-Delone-Krainov (ADK) model [4], the barrier suppression ionization (BSI) model [5] and the Keldysh-Faisal-Reiss (KFR) model ([3], and references therein), are probably the more prominent ones. In the ADK model the electron is assumed to tunnel in a quasistatic fashion through the potential barrier that arises from the distortion of the attractive potential of the ionic core by the external field. In the BSI model, this distortion is so strong that the barrier height drops below the energy level of the outermost electron so that it can escape immediately. The KFR model is based on S-matrix theory and describes a transition form the target's initial state to a final state dressed by the laser field, which can be either a plane wave or include corrections for the long-range Coulomb interaction.

However, there are difficulties to include specific molecular and atomic properties into these models, e.g. to account for substantially different ionization behavior of particles with the same ionization energy (IE). Recently, the latter raised considerable interest [6–8] due to the fact that the O_2 molecule (IE = 12.09 eV) starts to ionize at higher intensities than the Xe atom (IE = 12.13 eV), a phenomenon often called suppressed ionization. Quite contrary, the ionization behavior of the N_2 molecule (IE = 15.58 eV) and the Ar atom (IE = 15.76 eV) are observed to be almost identical [9,10]. Furthermore, tunneling models cannot retrieve the multiphoton ionization (MPI) behavior at low intensities, where the ionization probability is proportional to I^{m_0}, m_0 being the minimum number of photons required for a transition from the ground state to the ionization continuum (the so-called threshold order) [11].

In this paper, we present an heuristic model of intense-field photoionization which covers both linear and circular polarization. Not containing any adjustable parameters, its predictions are in satisfactory agreement with reported experiments on intense-field ionization of both atoms and molecules, over a wide range of parameters such as pulse duration, wavelength and ionization energy of the target particle.

This paper is organized as follows. After an introduction of the basic ingredients of the model, we first derive an iterative procedure to calculate ion yields, and present a simple analytic expression that closely approximates the results of this iteration. Then, we demonstrate the capability of our model to reproduce a large set of

[a] e-mail: hms@mpq.mpg.de

published experimental ion yields. After that, we demonstrate how our model explains suppressed ionization, and describe why certain target particles are poorly ionizing. We then discuss above-threshold ionization (ATI) spectra and nonsequential ionization for the case without electron recollision. Next, we give an alternative explanation of barrier suppression ionization (BSI). Then, we derive generalized multiphoton ionization (MPI) cross-sections, showing that our model's predictions are in agreement with Lambropoulos's scaling law [12,13], and we describe the influence of polarization on ion yields. After that, we discuss the observability of the threshold order of multiphoton ionization, and present an analysis of (multiple) photoionization of the C_{60} molecule. Finally, we elucidate our model in the framework of time-dependent perturbation theory in an Appendix.

2 The model

Figure 1 summarizes the present model. We consider a particle with ionization energy IE that is exposed to laser photons of energy $E_{\rm ph}= h/T$. The intensity of the corresponding mode-locked laser pulse with carrier frequency $1/T$ and linear or circular polarization is modeled for $0 \le t \le NT$ by

$$I(t) = \begin{cases} 1.94\, I_{\rm e} \cos^2\!\left(\dfrac{2\pi t}{T}\right) \sin^4\!\left(\dfrac{\pi t}{NT}\right) & \text{(lin. pol.)}; \\ 0.97\, I_{\rm e} \sin^4\!\left(\dfrac{\pi t}{NT}\right) & \text{(circ. pol.)}, \end{cases} \tag{1}$$

where N is the number of optical cycles in the $\sin^4$ pulse envelope and $I_{\rm e}$ is the experimental pulse intensity, defined as the ratio of fluence $\Phi = \int I(t')dt'$ and full-width-at-half-maximum pulse duration $\Delta_{\rm FWHM} = 0.364NT$. We chose the $\sin^4$ profile mainly because it has a finite pulse duration (unlike the often encountered Gaussian or sech^2 profiles), which conveniently limits the number of iterations required in our calculations (see Eq. (7) below). The exact functional form of the intensity envelope is not expected to affect the results presented here.

All energy levels E_m with $E_m = mE_{\rm ph} > IE$ (m is a positive integer) are in the continuum and can give rise to ionization. Level m is assumed to contribute when at least the required amount of photon energy E_m is absorbed within a short time interval given by $\Delta t_m = h/E_m = T/m$. The latter we call *timelet*. It is a measure for the shortest electronic response time. Within this time interval — in the so called impulsive limit — the system is unable to alter its state upon the photobombardment, and we ad hoc postulate that the target system can not distinguish between individual photons, i.e. that m photons of energy $E_{\rm ph}$ arriving within a typical electronic response time are effectively equivalent to a single photon of energy $mE_{\rm ph}$. Hence, we employ for either excitation mechanism the single-photon cross-section σ_m which connects the ground state of the target system to the virtually excited state m with a single photon of energy E_m. Via the use of the σ_m the individual properties of atoms and molecules enter the model.

Accordingly, the mean number of absorbed photons at level m within Δt_m is given by

$$M_m(t) = \frac{\sigma_m}{E_{\rm ph}} \int_t^{t+\Delta t_m} I(t')dt'. \tag{2}$$

By means of the Poisson distribution we can evaluate the probability $P_m(t)$ of absorption of at least m photons for a given mean value $M_m(t)$. This gives the ionization probability via doorway level m at a given time in the laser pulse:

$$P_m(t) = \sum_{s=m}^{\infty} \frac{M_m(t)^s}{s!} \exp(-M_m(t)) = 1 - \frac{\Gamma(m, M_m(t))}{\Gamma(m)}. \tag{3}$$

Clearly, all continuum levels m with their individual timelets and cross-sections can contribute to ionization. Therefore, the total ionization probability is

$$P_{\rm tot}(t) = 1 - \prod_m (1 - P_m(t)). \tag{4}$$

The overall ionization probability Y is obtained by propagating the timelets corresponding to all energy levels m through the laser pulse. Unless the pulse is extremely short or powerful, only timelets centered around the intensity maxima at $t = n \times T/2$ ($n = 1, ..., 2N-1$) need to be considered for linear polarization — reminiscent of tunneling models [39], and in agreement with the recently observed asymmetry in the single-shot electron distribution with few-cycle pulses [40]. The integration in equation (2) then yields

$$M_{m,n,q} \;=\; C \left\{ \frac{1}{2} + \frac{m}{4\pi} \sin\!\left(\frac{2\pi}{m}\right) \cos\!\left(\frac{4\pi q}{m}\right) \right\} \sin^4\!\left(\frac{n\pi}{2N}\right) \quad \text{(lin. pol.)}, \tag{5}$$

with $C = 1.94\, I_{\rm e} \sigma_m h/m{E_{\rm ph}}^2$. The index q ($|q| < m/4$) allows for additional side timelets, which play a role only for very large m, e.g. in the case of CO_2 laser ionization. For circular polarization, there are no intensity peaks so ionization can take place more continuously, at times $t = n' \times T/m$ ($n' = 1, ..., mN-1$). The integration in equation (2) then yields

$$M_{m,n'} \;=\; \frac{C}{2} \sin^4\!\left(\frac{n'\pi}{mN}\right) \qquad \text{(circ. pol.)}. \tag{6}$$

Thus, for equal *experimental* intensities $I_{\rm e}$, circularly polarized radiation has only half the intensity but $m/2$ times more timelets in comparison to linearly polarized radiation. If two or more timelets happen to coincide in time, they are evaluated in order of decreasing m. This preferential treatment of the fastest level becomes important under saturation conditions for nonsequential (NS) ionization phenomena or ATI spectra.

After labeling all conceivable timelets with a universal index $k = 1, 2, ..., K$ that orders them in time, and denoting the probability that the particle is ionized (remains

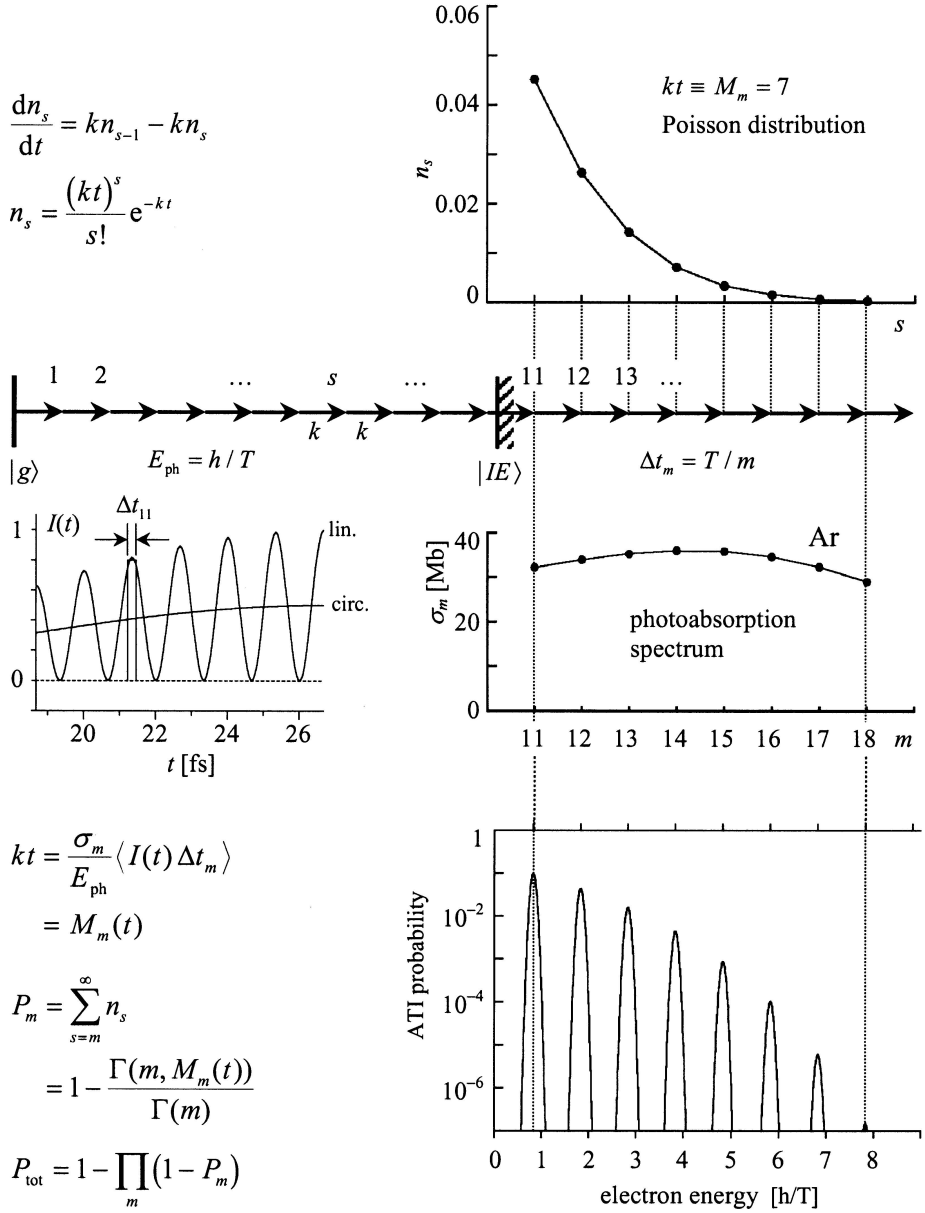

Fig. 1. Basic principles of the S.P.I. model. The arrows represent a general multi (s) photon process; m are ionizing levels. As indicated, the Poisson distribution can be derived from a general ladder climbing process. The example is based on the ionization of Ar (IE = 15.76 eV), which requires at least 11 photons of 800-nm radiation ($E_{\rm ph}$ = 1.55 eV, T = 8/3 fs, NT = 30 fs, $I_{\rm e} = 1.15 \times 10^{14}$ W/cm^2, $\Delta t_m(m = 11) = 8/33$ fs). For more information see text.

neutral) after the kth timelet by $Y_k^{\rm ion}$ ($Y_k^{\rm neut}$), we can write recursive expressions from which the final ionization probability Y follows as $Y_{k=K}^{\rm ion}$:

$$\begin{cases} Y_k^{\rm ion} = Y_{k-1}^{\rm ion} + \left(1 - \dfrac{\Gamma(m, M_k)}{\Gamma(m)}\right) Y_{k-1}^{\rm neut}, & Y_0^{\rm ion} = 0 \\ Y_k^{\rm neut} = \dfrac{\Gamma(m, M_k)}{\Gamma(m)} Y_{k-1}^{\rm neut}, & Y_0^{\rm neut} = 1. \end{cases} \tag{7}$$

Summarizing, the model describes the transition probability from a well-defined ground state into a well-defined state of the ionization continuum as a transient MPI process, confined to a time interval on the order of the electronic response time, and characterized by the oscillator strength of the direct transition. In this way, multiphoton ionization, optical field ionization and ionization by a fast charged particle for forward scattering bear close similarities. In the optical limit (zero momentum transfer) the interaction of a fast charged particle with a target particle is determined by the optical oscillator strength $f(0)$, which is in a simple way related to the single-photon cross-section $\sigma(E)$ for absorption of radiation. The fact that the electric fields involved in such an interaction are

comparable to the ones produced by intense lasers used in photoionization experiments hints at a key role of $\sigma(E)$ in modeling the outcomes of such experiments as well. The model does not involve any tunneling aspects nor shifting of electronic states. In particular, it does not consider dressed states; it is assumed that a typical time for ionization is smaller than a typical inverse Rabi frequency governing the population of such states. A more rigorous discussion is given in the Appendix.

Before applying our model, we wish to give a number of comments on the employed photoabsorption spectra. The single-photon absorption cross-sections σ_m or photoabsorption spectra are well documented in the literature [14–33]. They are either measured directly using tunable synchrotron radiation or by inelastic scattering of fast electrons for forward scattering or zero momentum transfer [34]. This technique is called dipole (e, e) spectroscopy. Furthermore, analytic formulas to calculate cross-sections are available [35]. The photoabsorption spectra usually exhibit sharp structures due to quasi-discrete, autoionizing or autodissociative Rydberg states and vibrational progressions (so-called superexcited states [36]). These overlap the true continuum states [14], which are responsible for direct ionization. Therefore, we determined the photoabsorption cross-sections through interpolation of the smooth continuum. The values thus obtained were then multiplied by ionization quantum yields [36] from literature. In this way, we exclude all resonant contributions. We also explicitly exclude any population of superexcited states, the presence of which might easily be detected because they often decay into fluorescing neutral fragments [37]. This procedure may need refinement if the dynamics of superexcited molecules is modified in the intense external laser field. Finally, we are aware that we employ only the single-photon accessible ionization continuum, thus ignoring selection rules; yet, this simplification together with our model assumptions is heuristically justified by the good agreement between theory and experiment (see below and Fig. 2). Clearly, we propose a mechanism complementary to high-harmonic generation, namely high-harmonic absorption. In support of our approach, a formal correlation between single-photon and multiphoton cross-sections can be derived in first-order Keldysh-Faisal-Reiss theory [38].

3 Analytic expression for the ionization probability

If none of the timelets appreciably depletes the ground state one can obtain an analytic approximation for Y

$$Y \approx 1 - \prod_m \left(\frac{\Gamma(m, mI_e/I_{\mathrm{sat},m})}{\Gamma(m)} \right)^{\frac{N}{\pi\sqrt{2}}\left(1-\frac{1}{m}\right)} \quad (8)$$

$$I_{\mathrm{sat},m} \equiv \frac{m^2 {E_{\mathrm{ph}}}^2}{1.94\,\sigma_m h} = \left(2.00 \times 10^{13} \frac{\mathrm{W}}{\mathrm{cm}^2} \right) \frac{E_m(\mathrm{eV})^2}{\sigma_m(\mathrm{Mbarn})}. \quad (9)$$

$I_{\mathrm{sat},m}$ corresponds to an ionization probability of ~ 0.5 at the pulse maximum ($M_{m,n=N,q=0} \approx m$ in Eq. (5); neglect the curly-bracketed factor, which varies between 0.5 and unity). In all cases of practical interest, the results from equations (7, 8) are hardly distinguishable. In the given form, equation (8) is valid for linear polarization; for circular polarization, $I_{\mathrm{sat},m}$ has to be replaced by $2I_{\mathrm{sat},m}$ and the exponent $N(1-1/m)/\pi\sqrt{2}$ by $N\sqrt{m/2\pi}$.

4 Comparison with experiments

The predictive power of our statistical photoionization (S.P.I.) model is demonstrated in Figure 2. It shows a compilation of all cases where we could bring together both experimental ion yields and photoabsorption cross-sections. Some representative results from other theories are also included. Each published yield vs. intensity curve is represented by a single characteristic intensity. To this end, the intersection method [11] was applied to determine absolute ion yields from the experimental data curves. We then took the lowest reliable ion yield for each experiment as the point of reference.

Going down in Figure 2 from benzene (9.24 eV, 3.7×10^{10} W/cm^2) to Ne^{3+} (97.12 eV, 3×10^{16} W/cm^2), we perceive no systematic deviations, except for some CO_2 laser experiments (10.6 μm, 2.6 ns, Ref. [41]), which might be due to experimental difficulties, for the measurements of reference [42] that are based on a novel way to determine saturation intensities, and for the Ar^{2+} ionization, which we discuss in detail below. Excluding these cases from an error distribution for $\log_{10}(I_{\mathrm{S.P.I.}}/I_{\mathrm{expt}})$, the expectation is 0.01 decade and the variance 0.27 decade. No correlation exists between the error and the Keldysh adiabaticity parameter [1], which up to now has drawn the line between the applicability of multiphoton and field ionization models. No other photoionization model currently spans this broad a parameter range except full ab initio calculations. This, in combination with its simple analytic formulation makes the S.P.I. model very attractive.

Faisal and coworkers have recently reported on total ionization rates and ion yields of noble gas atoms at high laser intensities [3]. Using a Coulomb-corrected Keldysh-Faisal-Reiss (KFR) rate formula they find good agreement with 36 experimental data sets assuming factors of up to two for the uncertainties in experimental intensities. Within similar limits, the saturation intensities predicted by the S.P.I. model are in satisfactory agreement with the calculations of Becker et al. and, hence, with the experimental data compiled by them.

5 Suppressed ionization

Figure 3 shows that the S.P.I. model correctly predicts the experimental observations also for the challenging ionization behavior of O_2 vs. Xe and N_2 vs. Ar. It shows Xe^+/O_2^+ yields (left panels) and Ar^+/N_2^+ yields (right panels) as a function of intensity for 800-nm pulses of different pulse durations: 30 fs (top panels, experimental data from Ref. [10]) and 200 fs (bottom panels, experimental data from Ref. [9]). Although our model somewhat

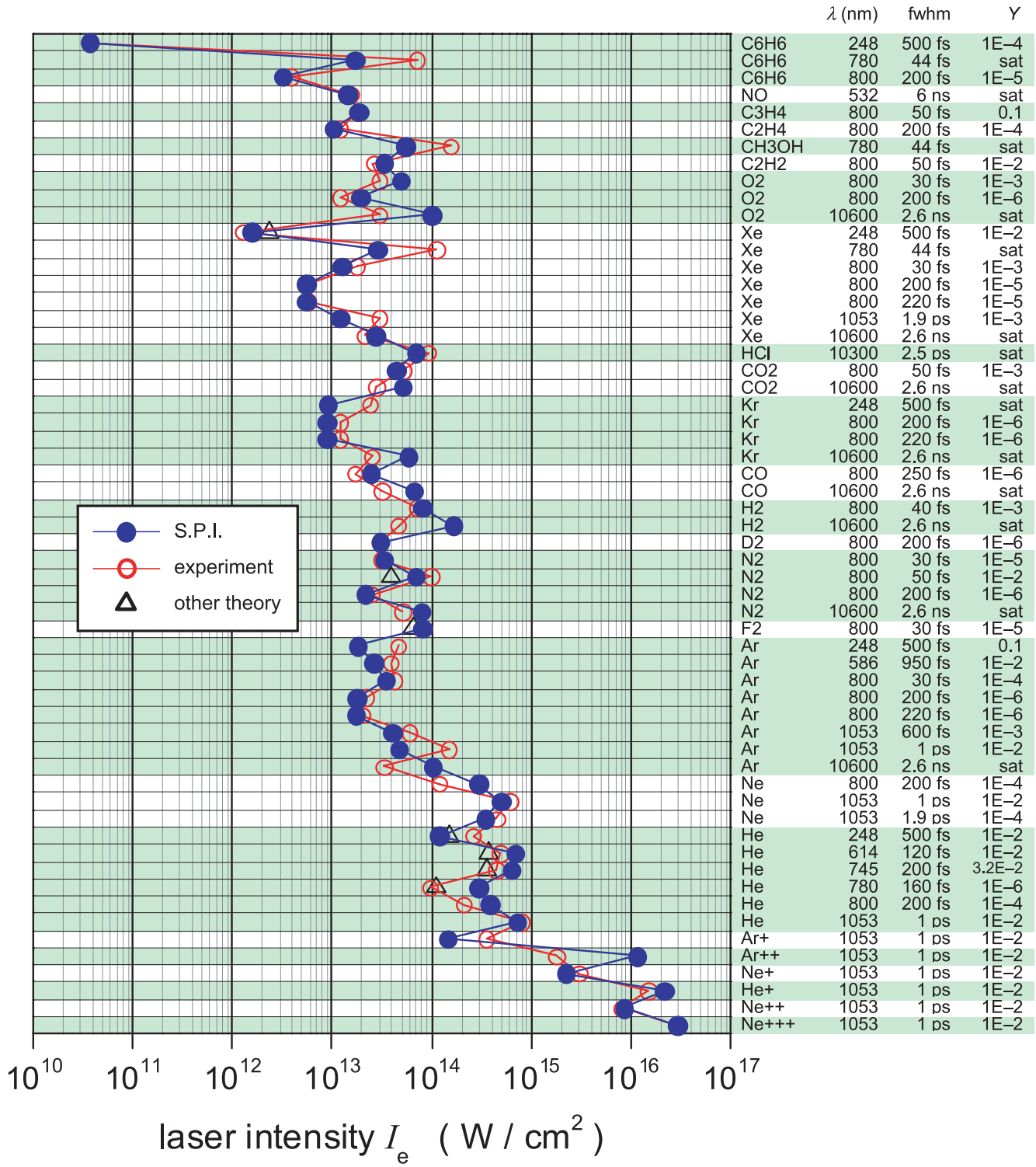

	λ (nm)	fwhm	Y
C6H6	248	500 fs	1E–4
C6H6	780	44 fs	sat
C6H6	800	200 fs	1E–5
NO	532	6 ns	sat
C3H4	800	50 fs	0.1
C2H4	800	200 fs	1E–4
CH3OH	780	44 fs	sat
C2H2	800	50 fs	1E–2
O2	800	30 fs	1E–3
O2	800	200 fs	1E–6
O2	10600	2.6 ns	sat
Xe	248	500 fs	1E–2
Xe	780	44 fs	sat
Xe	800	30 fs	1E–3
Xe	800	200 fs	1E–5
Xe	800	220 fs	1E–5
Xe	1053	1.9 ps	1E–3
Xe	10600	2.6 ns	sat
HCl	10300	2.5 ps	sat
CO2	800	50 fs	1E–3
CO2	10600	2.6 ns	sat
Kr	248	500 fs	sat
Kr	800	200 fs	1E–6
Kr	800	220 fs	1E–6
Kr	10600	2.6 ns	sat
CO	800	250 fs	1E–6
CO	10600	2.6 ns	sat
H2	800	40 fs	1E–3
H2	10600	2.6 ns	sat
D2	800	200 fs	1E–6
N2	800	30 fs	1E–5
N2	800	50 fs	1E–2
N2	800	200 fs	1E–6
N2	10600	2.6 ns	sat
F2	800	30 fs	1E–5
Ar	248	500 fs	0.1
Ar	586	950 fs	1E–2
Ar	800	30 fs	1E–4
Ar	800	200 fs	1E–6
Ar	800	220 fs	1E–6
Ar	1053	600 fs	1E–3
Ar	1053	1 ps	1E–2
Ar	10600	2.6 ns	sat
Ne	800	200 fs	1E–4
Ne	1053	1 ps	1E–2
Ne	1053	1.9 ps	1E–4
He	248	500 fs	1E–2
He	614	120 fs	1E–2
He	745	200 fs	3.2E–2
He	780	160 fs	1E–6
He	800	200 fs	1E–4
He	1053	1 ps	1E–2
Ar+	1053	1 ps	1E–2
Ar++	1053	1 ps	1E–2
Ne+	1053	1 ps	1E–2
He+	1053	1 ps	1E–2
Ne++	1053	1 ps	1E–2
Ne+++	1053	1 ps	1E–2

Fig. 2. Comparison of predictions of the S.P.I. model (blue solid circles) to experimental (red open circles) and representative theoretical (triangles) results. Each row in the diagram corresponds to a separate experiment, with the target particle, laser wavelength and pulse duration indicated. The given intensities produce the indicated ion yields Y ('sat' = saturation). The S.P.I. intensities have been calculated with equation (8). Solid lines guide the eye. The adjacent table gives the employed cross-sections and references.

Table 1. Cross-sections and references employed in Figure 2. First column: target particle; column labeled m_0: lowest order taken into account; column labeled $\sigma_{m_0}, \sigma_{m_0+1}, ...$: cross-sections used (in Mb = 10^{-18} cm^2).

		m_0	$\sigma_{m_0}, \sigma_{m_0+1}, ...$	Ref.
C_6H_6	(248 nm, 500 fs)	2	28, 108, 132	[67,15]
C_6H_6	(780 nm, 44 fs)	6	14, 41, 68, 82, 130, 157, 144	[42,15,16]
C_6H_6	(800 nm, 200 fs)	6	6, 36, 67, 71, 125, 144, 143	[68,15,16]
NO	(532 nm, 6 ns)	5	4.3, 10.4, 16.4, 22.5	[69,17]
C_3H_4	(800 nm, 50 fs)	7	42, 37, 41, 64, 74, 71, 57	[70,18]
C_2H_4	(800 nm, 200 fs)	7	8, 19, 45, 56, 59	[71,19]
CH_3OH	(780 nm, 44 fs)	7	6, 20, 31, 43, 46, 47, 46, 42, 37	[42,72]
C_2H_2	(800 nm, 50 fs)	8	21.4, 22.6, 34, 30.6, 28.3	[70,20]
O_2	(800 nm, 30 fs)	8	3, 5, 11, 30, 24, 27, 27	[73,21]
O_2	(800 nm, 200 fs)	8	3, 5, 11, 30, 24, 27, 27	[9,21]
O_2	(10.6 μm, 2.6 ns)	111,144	20, 35	[41,21]
Xe	(248 nm, 500 fs)	3	59.8	[74,22]
Xe	(780 nm, 44 fs)	8	26.3, 62.2, 57.0	[42,22]
Xe	(800 nm, 30 fs)	8	19.9, 63.3	[10,22]
Xe	(800 nm, 200 fs)	8	19.9, 63.3	[75,22]
Xe	(800 nm, 220 fs)	8	19.9, 63.3	[76,22]
Xe	(1053 nm, 1.9 ps)	11	39.0, 62.3, 59.0	[53,22]
Xe	(10.6 μm, 2.6 ns)	104	65	[41,22]
HCl	(10.3 μm, 2.5 ps)	120	45	[77,23]
CO_2	(800 nm, 50 fs)	9	12, 14.8, 30.8, 33, 36.2, 36.1	[70,24,25]
CO_2	(10.6 μm, 2.6 ns)	118	45	[41,24,25]
Kr	(248 nm, 500 fs)	3	44.4	[52,22]
Kr	(800 nm, 200 fs)	10	45.4, 44.9	[75,22]
Kr	(800 nm, 220 ns)	10	45.4, 44.9	[76,22]
Kr	(10.6 μm, 2.6 ns)	120	45	[41,22]
CO	(800 nm, 250 fs)	10	13.6, 22.6, 22.5, 22, 22.15, 21.6, 21	[78,14,26]
CO	(10.6 μm, 2.6 ns)	120	36	[41,14,26]
H_2	(800 nm, 40 fs)	10	13.5, 11, 9.1, 7.5, 6.3	[79,27,28]
H_2	(10.6 μm, 2.6 ns)	132	18	[41,29]
D_2	(800 nm, 200 fs)	10	13.5, 11, 9.1, 7.5, 6.3 (values for H_2)	[80,27,28]
N_2	(800 nm, 30 fs)	11	26.4, 23.5, 23.1, 22.7, 25.2, 23.5	[73,30,31]
N_2	(800 nm, 50 fs)	11	26.4, 23.5, 23.1, 22.7, 25.2, 23.5	[70,30,31]
	other theory:			[81]
N_2	(800 nm, 200 fs)	11	26.4, 23.5, 23.1, 22.7, 25.2, 23.5	[9,30,31]
N_2	(10.6 μm, 2.6 ns)	136	40	[41,31]
F_2	(800 nm, 30 fs)	11	6, 8, 17, 22, 23, 23	[45]
	other theory:			[7]
Ar	(248 nm, 500 fs)	4	35.7, 34.3	[52,22]
Ar	(586 nm, 950 fs)	8	32.5, 35.1	[82,22]
Ar	(800 nm, 30 fs)	11	32.8, 34.7	[10,22]
Ar	(800 nm, 200 fs)	11	32.8, 34.7	[75,22]
Ar	(800 nm, 220 fs)	11	32.8, 34.7	[76,22]
Ar	(1053 nm, 600 fs)	14	31.7, 33.9	[51,35]
Ar	(1053 nm, 1 ps)	14	31.7, 33.9	[5,35]
Ar	(10.6 μm, 2.6 ns)	135	30.5	[41,22]
Ne	(800 nm, 200 fs)	14	6.45, 7.18, 7.88, 8.28	[75,32]
Ne	(1053 nm, 1 ps)	19	6.67, 7.43, 7.48, 8.18, 8.51	[5,35]
Ne	(1053 nm, 1.9 ps)	19	6.67, 7.43, 7.48, 8.18, 8.51	[53,35]
He	(248 nm, 500 fs)	5	7.27, 5.47	[52,33]
	other theory:			[83]
He	(614 nm, 120 fs)	13	6.83, 6.06, 5.43	[55,33]
	other theory:			[83]
He	(745 nm, 200 fs)	15	7.32, 6.63, 6.05	[84,33]
	other theory:			[83]
He	(780 nm, 160 fs)	16	7.21, 6.51	[85,33]
	other theory:			[83]
He	(800 nm, 200 fs)	16	7.52, 6.77	[75,33]
He	(1053 nm, 1 ps)	22	7.03, 6.50	[5,35]
Ar^+	(1053 nm, 1 ps)	24	43.8, 37.1, 31.7	[5,35]
Ar^{2+}	(1053 nm, 1 ps)	35	1.42	[5,35]
Ne^+	(1053 nm, 1 ps)	35	7.0, 7.4, 7.7, 8.0, 8.2, 8.3	[5,35]
He^+	(1053 nm, 1 ps)	47	1.50, 1.41, 1.34	[5,35]
Ne^{2+}	(1053 nm, 1 ps)	54	3.8, 4.7, 5.3, 5.7, 5.9, 6.1, 6.2, 6.2	[5,35]
Ne^{3+}	(1053 nm, 1 ps)	83	4.1, 4.0, 4.0, 3.9, 3.8	[5,35]

overestimates the Xe^+ yields, it reproduces the suppressed ionization of O_2 and its absence in N_2 very well. This is caused by the fact that the cross-sections of the first few continuum levels E_m are considerably smaller for O_2 than for Xe, whereas for the pair N_2/Ar there is no such marked difference (see data and reference in Tab. 1). A recent publication [7] discussed the suppressed ionization of O_2 and its absence in N_2 in terms of the symmetry of molecular wave functions. The S.P.I. model automatically comprises such symmetry arguments, because VUV cross-sections in the energy range just above the ionization threshold are strongly influenced by interference between the atomic sites in the molecule [43]. For example, the negative molecularity (or out-of-phase LCAO, see Ref. [43]) of the outer valenceorbitals of O_2 reduces its VUV cross-section in the first few eV above the ionization threshold. However, as soon as the inner-shell $\pi_u 2p(O_2)$ MO, which has positive molecularity (in-phase LCAO [43]), is reached, the O_2 VUV spectrum shows a marked increase. Because symmetry effects are automatically accounted for in our model, no knowledge of wave functions is required. This appears to be a major advantage of our approach, especially for more complicated polyatomic molecules, for which atomic and ionic wave functions may not be readily available. Parenthetically, reference [7] puts forward a somewhat different view of what MO types lead to suppressed ionization: reference [7] ascribes it to the antibonding character of the valence orbital, but in the S.P.I. model it is a built-in consequence of the negative molecularity of MOs. A conflict between these two views arises for certain valence orbitals, the $3\sigma_g(N_2)$ orbital being an important example: this MO is bonding, but it is also an out-of-phase LCAO (negative molecularity): $3\sigma_g(N_2) \propto 2p_z(N_A) - 2p_z(N_B)$. Thus, it is not expected to give rise to suppressed ionization by reference [7], but in the S.P.I. model there can be suppression for a properly chosen wavelength. Just above the ionization threshold $(3\sigma_g)^{-1}$ the single-photon absorption cross-section of N_2 starts off below 10 Mb, growing to values on the order of 25 Mb only when the $(1\pi_u)^{-1}$ edge is reached [14]. This low cross-section energy region, however, is fairly narrow (in O_2 it is about three times wider) and with 800-nm radiation no continuum level E_m happens to fall in it. At 825 nm, E_{11} would be at 16.5 eV where the cross-section is low, so that suppressed ionization should be observable at that wavelength in N_2. Strikingly, in reference [7], the calculated N_2^+ yields (based on the bonding character of the $3\sigma_g(N_2)$ orbital) are larger than the calculated Ar^+ yields, at variance with the experimental data. The S.P.I. model correctly predicts the Ar^+ yields to exceed the N_2^+ yields (see Fig. 3). Recent experiments [44] using 790-nm, 100-fs pulses do not show suppressed ionization in F_2, contrary to the predictions of both references [6,7]. However, these experiments also show a slight enhancement for N_2^+ relative to Ar^+ at variance with references [9,10] and with the present model. Unfortunately, experimental values of the VUV cross-sections needed in our model are not available. Calculations suggest [45] that F_2, like O_2, has a small (few Mb) single-photon cross-section just above the ionization threshold, which then rises to roughly 20 Mb when the $\pi_u 2p(F_2)$ MO is reached. Using these calculated values we fully confirm the predicted [7] suppressed ionization in F_2 with 800-nm, 30-fs pulses (see Fig. 2). It must be kept in mind, however, that there is confusion about the exact value of the cross-section of F_2 just above its ionization threshold (see Ref. [45], and references therein), which makes our results correspondingly uncertain. Interference-induced dynamical variations in the photoabsorption are generally called 'Cooper minima' [14,46]. Hence, we use the term 'Cooper suppressed ionization' for what is usually called suppressed ionization in molecules. In view of the S.P.I. model the true fingerprint of Cooper suppressed ionization would be a reduced strength of the first few ATI peaks in the electron spectrum.

6 Poorly ionizing species

Even atoms may exhibit suppressed ionization, if there is only little oscillator strength just above the ionization threshold, followed by a significant rise at higher energies. Previously, 500-fs KrF laser ionization of sputtered neutral atoms was investigated [47]. The surprisingly weak Mg (IE = 7.65 eV) ion signal and the absence of Na (IE = 5.14 eV) ions become understandable within the S.P.I. framework, since the photoabsorption cross-sections at 10 eV (2 photons) are extremely small (0.4 Mb for Mg, 0.1 Mb for Na [35]). Owing to their low IE and photoabsorption cross-section, alkali atoms should be ideal objects to investigate field-dominated ionization.

7 ATI spectra

Equation (3) mimics the abundance of the direct ATI electrons. This is shown in the lower panel of Figure 1. The decline of the ATI spectrum is due to the fact that the peaks represent successively higher order processes. Increasing the intensity above the saturation threshold ($M \approx m - 1/e$) would shift the Poisson distribution accordingly, which results in a broader distribution with a distinct energy maximum.

Photoelectrons that form via a continuum level m have kinetic energy $E_{\rm kin} = E_m - IE$. By monitoring the contributions from each individual level, we can predict the corresponding ATI photoelectron spectra, that are characteristic for high-intensity ionization processes. For linear polarization, and far below saturation (for the general case, see Eqs. (7)), we find for the ATI spectrum

$$P_{\rm ATI}(E_{\rm kin} = E_m - IE) \approx 1 - \left(\frac{\Gamma(m, mI_e/I_{{\rm sat},m})}{\Gamma(m)}\right)^{\frac{N}{\pi\sqrt{2}}\left(1-\frac{1}{m}\right)} . \quad (10)$$

This kinetic energy spectrum more or less mimics the structure of the single-photon absorption spectrum (weighted by the high-energy tail of the Poisson distribution), in the sense that small cross-sections induce weak

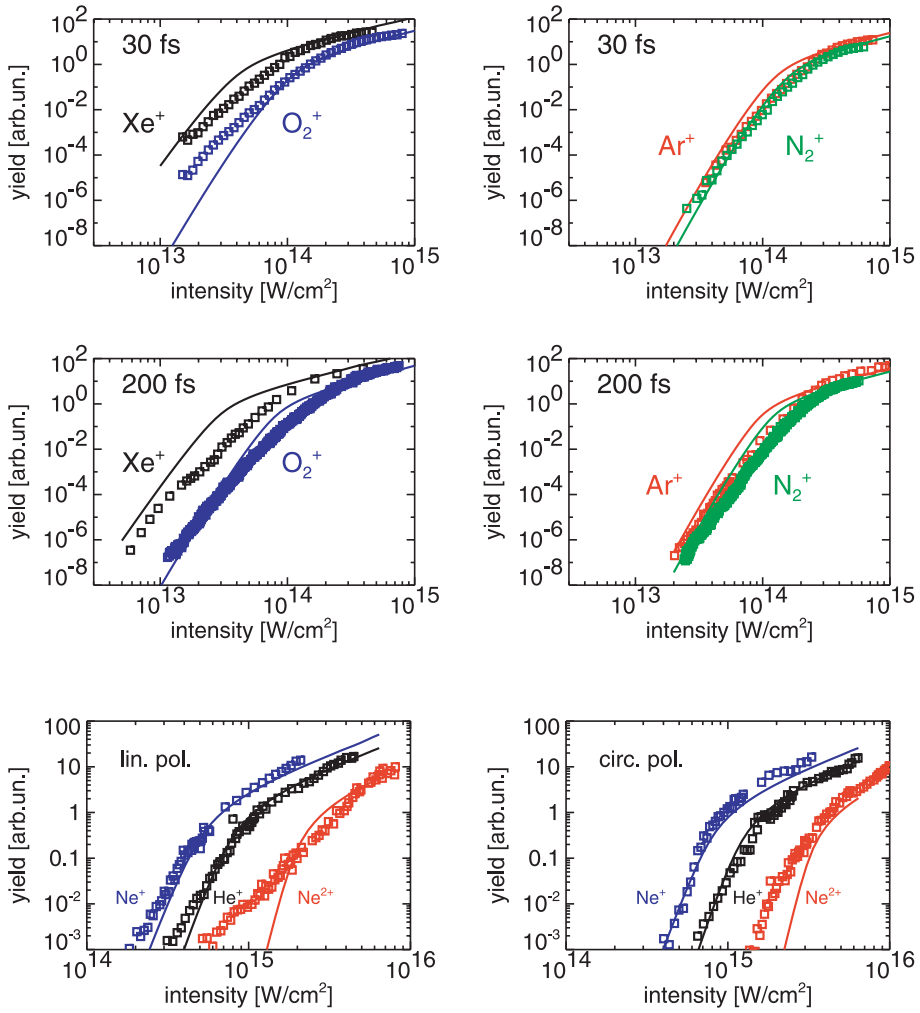

Fig. 3. Ionization behavior of Xe(black)/O_2(blue) and Ar(red)/N_2(green) upon irradiation with a linearly polarized, 800-nm pulse. Upper panels: pulse duration 30 fs (experimental data from Ref. [10]); lower panels: 200 fs (experimental data from Ref. [9]). Solid lines: present model, equation (8), volume integrated. The curves in the lower right panel were obtained by multiplying the original intensities by a factor of 1.25; for the other panels, this multiplication factor was 1.0 (no correction).

Fig. 4. Ionization of He and Ne using linearly polarized (left panel) and circularly polarized (right panel) 120-fs pulses of 614-nm wavelength: He^+ yield: black, Ne^+ yield: blue, Ne^{2+} yield: red. Solid curves: present model, equation (8), volume integrated, original intensities divided by a factor of 1.56. Experimental data from reference [55].

ATI peaks and large cross-sections induce strong ATI peaks (note that $I_{\mathrm{sat},m}^{-1} \propto \sigma_m$). Figures 5 and 6 illustrate this. In Figure 5 we show single-photon cross-sections of the atoms He, Ar, and O; these values were calculated using the analytic approximations given in reference [35]. The He cross-section has its maximum right at the ionization threshold. The cross-section of the Ar atom reaches its maximum about 7 eV above the ionization threshold, but the cross-sections in the first 7 eV are not much lower ($> 85\%$). For the O atom the maximum is reached about 10 eV above the ionization threshold, but in this case the value just above the threshold is only 16% of the maximum value. Figure 6 shows ATI spectra for these three atoms, calculated using equations (7), at their indicated saturation intensities. These spectra give the contribution of each level m to the total ion yield. The He spectrum is strongly peaked at low kinetic energies. The Ar spectrum is also strongest in the lowest level but broader than the He spectrum. A strong suppression of the first few ATI peaks is seen in the O atom. This atom can be taken here as a substitute for the O_2 molecule, whose single-photon cross-section has essentially the same features. The weak onset of the cross-section of the O atom renders its first few channels ineffective. One may conclude that the true signature of Cooper suppressed ionization is a suppression of the first few ATI peaks, so that most electrons are created with considerable excess energy. This inhibits electron recollision effects such as the formation of ATI plateaus [48], high-harmonics generation, and NS ionization [49]. In this way the S.P.I. model rationalizes corresponding experimental observations [50].

8 Nonsequential ionization

The S.P.I. model naturally predicts sequential (stepwise) ionization processes:

$$\mathrm{A} \xrightarrow{\sigma_1;\, m_1 E_{\mathrm{ph}}} \mathrm{A}^+ \xrightarrow{\sigma_2;\, m_2 E_{\mathrm{ph}}} \mathrm{A}^{2+}.$$

An example is the sequence Ne, Ne^+, Ne^{2+}, Ne^{3+} in Figure 2. Each channel has been treated individually. However, multiply charged ions can also form via nonsequential ionization processes, e.g., the direct freeing of two electrons from the precursor state:

$$\mathrm{A} \xrightarrow{\sigma_1;\, (m_1+m_2) E_{\mathrm{ph}}} \mathrm{A}^{2+}.$$

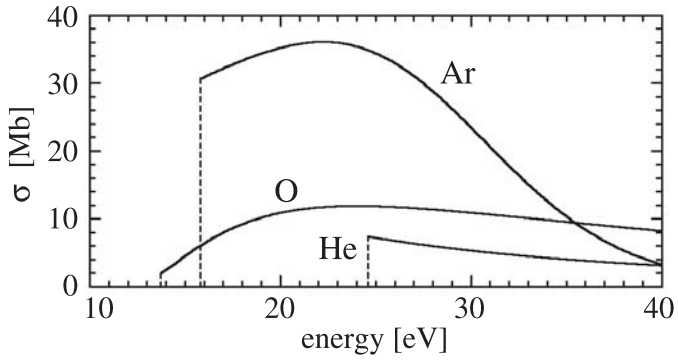

Fig. 5. Single-photon cross-sections of He, Ar, and O, calculated from reference [35].

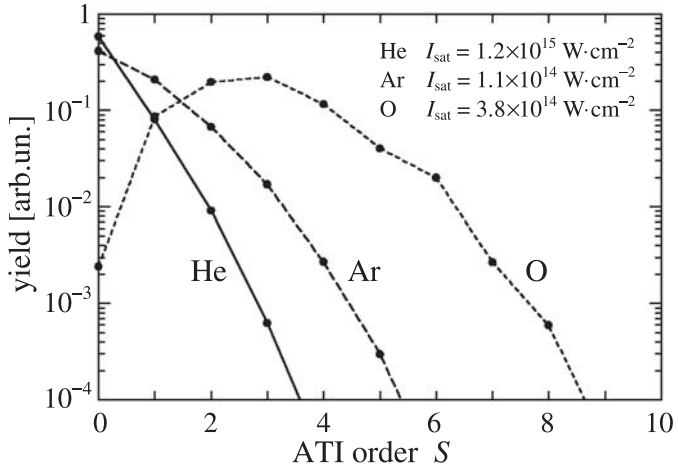

Fig. 6. Calculated ATI spectra of He, Ar, and O. The spectra were calculated at the indicated saturation intensities, for which the total ionization probability is $1 - 1/e \approx 0.63$. No volume integration.

This is also a viable mechanism in the S.P.I. model, owing to the high-energy tail of the Poisson distribution. Using equation (9), we find for the ratio of saturation intensities

$$\frac{I_{\rm sat}^{\rm NS}}{I_{\rm sat}^{\rm seq}} = \left(\frac{\sigma_2}{\sigma_1}\right) \frac{IE_1(IE_1 + IE_2)}{IE_2^2} \approx \frac{3}{4}\left(\frac{\sigma_2}{\sigma_1}\right). \qquad (11)$$

Here we have used $IE_2 \approx 2\,IE_1$, which holds in many cases. Because σ_2 is usually smaller than σ_1 (for He, $\sigma_1 = 7.5$ Mb [33] and $\sigma_2 = 1.5$ Mb [35]), NS ionization precedes sequential ionization on the intensity scale. This is in agreement with the experimentally observed 'knees' in the ion yields of multiply charged species [5,51]. Moreover, also the fact that the calculated intensity for the $Ar^{2+} \rightarrow Ar^{3+}$ sequential ionization is far beyond the value of Chin and coworkers [5,51] (see Fig. 2) can be resolved in terms of a NS channel contributing to the experimental ion yield: consulting the S.P.I. model on the NS formation of Ar^{3+} via Ar^+, we find that early NS appearance of Ar^{3+} is indeed expected (cf. Eq. (11)), because the Ar^+ absorption cross-section is exceptionally high (about 40 Mb [35]). To quantify NS ionization in the S.P.I. model, we consider six processes P1–P6 (seq = sequential):

$$\begin{aligned}
&\mathrm{P1, seqAr} &&\longrightarrow \mathrm{Ar}^+ && (14 \le s \le 38, \sigma_{14}^{\rm Ar})\\
&\mathrm{P2, NSAr} &&\longrightarrow \mathrm{Ar}^{2+} && (39 \le s \le 73, \sigma_{14}^{\rm Ar})\\
&\mathrm{P3, seqAr}^+ &&\longrightarrow \mathrm{Ar}^{2+} && (24 \le s \le 58, \sigma_{24}^{\rm Ar+})\\
&\mathrm{P4, NSAr}^+ &&\longrightarrow \mathrm{Ar}^{3+} && (s \ge 59, \sigma_{24}^{\rm Ar+})\\
&\mathrm{P5, NSAr} &&\longrightarrow \mathrm{Ar}^{3+} && (s \ge 74, \sigma_{14}^{\rm Ar})\\
&\mathrm{P6, seqAr}^{2+} &&\longrightarrow \mathrm{Ar}^{3+} && (s \ge 35, \sigma_{35}^{\rm Ar2+}), \qquad (12)
\end{aligned}$$

where the required number of photons s and the relevant single-photon cross-section are indicated for each process. Labeling the timelets with $k = 1, 2, ..., K$ as before, and writing p_i for the S.P.I. ionization probability of process Pi due to timelet k, and n_k^{Q+} for the probability to find Ar^{Q+} after timelet k, we calculate the distribution of charge states in an iterative way:

$$\begin{aligned}
n_k^{3+} &= n_{k-1}^{3+} + p_5 n_{k-1}^{0} + p_4 n_{k-1}^{1+} + p_6 n_{k-1}^{2+}\\
n_k^{2+} &= n_{k-1}^{2+} + p_2 n_{k-1}^{0} + p_3 n_{k-1}^{1+} - p_6 n_{k-1}^{2+}\\
n_k^{1+} &= n_{k-1}^{1+} + p_1 n_{k-1}^{0} - p_3 n_{k-1}^{1+} - p_4 n_{k-1}^{1+}\\
n_k^{0} &= n_{k-1}^{0} - p_1 n_{k-1}^{0} - p_2 n_{k-1}^{0} - p_5 n_{k-1}^{0} \qquad (13)
\end{aligned}$$

with the initial values $n_{k=0}^0 = 1$ and $n_{k=0}^{1+} = n_{k=0}^{2+} = n_{k=0}^{3+} = 0$. Equation (13) adds all probabilities to reach Ar^{Q+} from lower charge states, through either sequential or nonsequential processes.

Figure 7 shows the resulting charge distributions as a function of peak intensity for $\lambda = 1053$ nm and pulse durations of 1.28 fs ($N = 1$ in Eq. (1), black curve), 10 fs (red), 50 fs (blue), 100 fs (green), and 500 fs (purple). Clearly, the use of a longer pulse pushes the NS contribution to the Ar^{3+} signal (due to process P4) down to a less observable level. For such pulse durations process P3 can largely deplete the Ar^+ ensemble before the intensity gets high enough to make P4 (which also starts from Ar^+) an efficient process. For shorter pulses (say, below 50 fs) there is less time for such a depletion, which results in a larger NS contribution to the Ar^{3+} signal. The gross features of Figure 7 are found in accordance with the observations of Chin and coworkers [5].

This analysis may be helpful to discriminate between the direct NS two-electron emission process and the recollision based process. It is clear that the direct process becomes more important for shorter pulses and higher intensities respectively, because higher intensities deplete the amount of appropriate (low initial energy) electrons. According to the Poisson distribution the yield of 'threshold' electrons and therefore the yield of recollision events goes through a maximum at $M_m = m$ with $P_{\max} \approx 1/\sqrt{2\pi m}$. This explains why the experimentally observed NS ionization curves (see e.g. Fig. 4) approach the 'direct' limit at high intensities or, vice versa, recollision events are more pronounced at lower intensities.

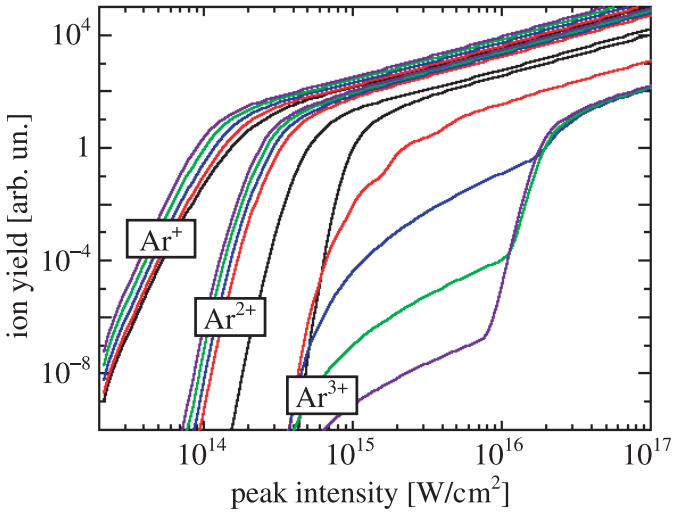

Fig. 7. Calculated volume-integrated ion yields of Ar with 1053-nm pulses as a function of peak intensity. The figure shows the influence of pulse duration on the NS contribution to the Ar^{3+} signal. Black curves: pulse duration 1.28 fs ($N = 1$ in Eq. (1)); red: 10 fs; blue: 50 fs; green: 100 fs; purple: 500 fs.

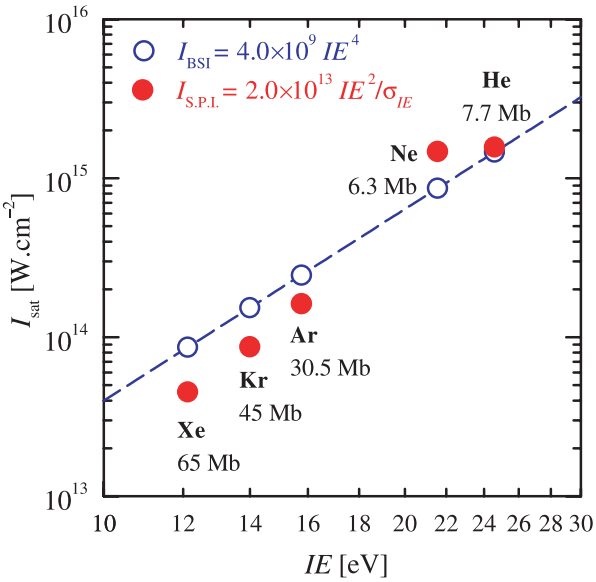

Fig. 8. Saturation intensities of the noble gases as a function of their ionization energy *IE*. Blue circles and dashed line: BSI model. Red solid circles: present S.P.I. model. The threshold cross-section $\sigma_{\rm IE}$ is indicated for each species. Note the double-logarithmic representation.

9 Comparison with the BSI model

We now compare the saturation intensity for the noble gases as predicted by the S.P.I. model (see Eq. (9)) and the popular BSI (barrier suppression ionization) model [5]. For practical use of equation (9), one has to choose the smallest ${E_m}^2/\sigma_m$ value in the ionization continuum, which for the noble gases occurs just above the ionization threshold ($E_m \approx IE$). Thus, from the S.P.I. model we obtain

$$I_{\rm sat}({\rm W/cm^2}) = 2.00 \times 10^{13}\ IE({\rm eV})^2/\sigma_{\rm IE}({\rm Mbarn}), \quad (14)$$

where $\sigma_{\rm IE}$ denotes the noble gas threshold cross-sections. In accordance with the BSI model, which predicts $I_{\rm sat}({\rm W/cm^2}) = 4.00{\times}10^9 IE({\rm eV})^4$, the saturation intensity is wavelength independent. Although the *IE* dependences are at challenging variance, the saturation intensities predicted by the two models are very similar, as Figure 8 shows. This is due to the fact that the noble gas threshold cross-sections $\sigma_{\rm IE}$ closely follow an IE^{-2} power law. However, contrary to BSI, the S.P.I. model is also in good agreement with species other than the noble gases (see Fig. 2). In terms of the electric field, equation (14) reads $E_{\rm sat}({\rm V/cm}) = 1.2 \times 10^8 IE({\rm eV})/\sqrt{\sigma_{\rm IE}({\rm Mbarn})}$.

10 Generalized cross-sections

At very low intensities, the first term of the sum in equation (3) dominates, and so the well-known MPI law [4] is retrieved: ionization probability $\propto I^m$. Hence, a comparison of ${M_m}^m/m!$ with the corresponding time-integrated rate equation enables us to extract a new generalized MPI cross-section:

$$\frac{\sigma^{(m)}_{\rm MPI}}{(\sigma_m)^m} = \frac{2^{m+1}/m}{m!}\left\{\frac{1}{2}+\frac{m}{4\pi}\sin\left(\frac{2\pi}{m}\right)\right\}^m \left(\frac{h}{mE_{\rm ph}}\right)^{m-1}. \quad (15)$$

As shown in Table 2, this compares favorably with Lambropoulos's scaling law [12,13] and also with experiments [52].

11 Circularly polarized light

Similarly, we find for the ratio of threshold intensities with linear and circular polarization

$$\frac{I^{\rm circ}_{\rm thr}}{I^{\rm lin}_{\rm thr}} = \left(\frac{2^{m+1}}{m}\right)^{1/m}\left\{\frac{1}{2}+\frac{m}{4\pi}\sin\left(\frac{2\pi}{m}\right)\right\}, \quad (16)$$

which has a numerical value between 1 and 2. Measured ratios for Xe (1053 nm, $m = 11$, Ref. [53]) and toluene (800 nm, $m = 6$, Ref. [54]) are 1.7 and 1.43; equation (16) predicts 1.67 and 1.52, respectively. The result in equation (16) is a consequence of the different intensity profiles (see Eq. (1)) and of our timelet definition, as contained in the curly-bracketed factor (compare Eqs. (5, 6)). Figure 4 shows He^+ (black), Ne^+ (blue), and Ne^{2+} (red) yields as a function of intensity using linearly (left panel) and circularly (right panel) polarized, 120-fs, 614-nm pulses. The solid curves are our present results, and the experimental data points were taken from reference [55]. The only feature that our calculations do not reproduce is the

Table 2. Generalized cross-sections of the noble gases for 248-nm radiation. Units: $[\sigma^{(n)}] = \mathrm{cm}^{2n}\,\mathrm{s}^{n-1}$.

Species	Present model	Scaling [12,13]	Experiment [52]
He: $(\sigma^{(5)})^{1/5}$	1.0×10^{-30}	0.6×10^{-30}	$(0.4\ ^{+0.24}_{-0.04}) \times 10^{-30}$
Ne: $(\sigma^{(5)})^{1/5}$	1.1×10^{-30}	0.8×10^{-30}	—
Ar: $(\sigma^{(4)})^{1/4}$	3.8×10^{-29}	1.8×10^{-29}	$(1.1\ ^{+0.1}_{-0.2}) \times 10^{-29}$
Kr: $(\sigma^{(3)})^{1/3}$	1.3×10^{-27}	0.4×10^{-27}	$(0.49^{+0.17}_{-0.10}) \times 10^{-27}$
Xe: $(\sigma^{(3)})^{1/3}$	1.7×10^{-27}	0.5×10^{-27}	$(1.7\ ^{+1.7}_{-0.9}) \times 10^{-27}$

enhanced Ne^{2+} yield for lower intensities, that causes a 'knee' structure in the experimental data. In so far as this nonsequential 'knee' is due to electron rescattering [49], it is not accounted for in our calculations. When radiation with long wavelengths is used, the order m is large. In that case, equation (16) predicts $I_{\mathrm{thr}}^{\mathrm{circ}}/I_{\mathrm{thr}}^{\mathrm{lin}} \to 2$, or, in terms of the electric field, $E_{\mathrm{thr}}^{\mathrm{circ}} \approx E_{\mathrm{thr}}^{\mathrm{lin}}$. In this sense the S.P.I. model lends some importance to the electric field for longer wavelengths, even though this field is not one of its underlying concepts.

12 Observability of the threshold order

The frequently observed bent ion yield curves (i.e. an ionization order that is smaller than the threshold MPI order) are usually taken as an indication of field-induced tunneling ionization because this particular shape can easily be reproduced by appropriately scaled Ammosov-Delone-Krainov (ADK) type formulas [4]. On the other hand, from the first term in equation (3) we also find a decreasing slope with increasing intensity, albeit somewhat less pronounced: $\mathrm{d}(\ln P)/\mathrm{d}(\ln M) = m - M$. For a relatively low order, say $m = 6$, and tolerating a decrease to a log-log slope of 5.5, we are at an ionization probability of 1.4×10^{-5} (see Eq. (3)). This means that the threshold MPI order can be observed. However, for $m = 16$ and $M = 0.5$, P is as small as 4.6×10^{-19}. This implies that the threshold MPI order can never be observed if it is too large. This statement can be further quantified by noticing that for an observation threshold of, say, 10^{-5} the slope $\mathrm{d}(\ln P)/\mathrm{d}(\ln M)$ at threshold deviates less than 0.5 from the MPI order m for $m \leq 6$. Taking 10 eV as a typical atomic or molecular *IE*, we conclude that visible and shorter wavelengths would typically lead to an MPI-like behavior, with a slope close to the lowest order, whereas near-infrared and longer wavelengths would typically lead to smaller slopes, seemingly indicating a tunneling process. This general conclusion is in agreement with the traditional notion, as expressed in the Keldysh parameter [1], that longer wavelengths are more likely to induce tunneling ionization than shorter ones. However, the Keldysh parameter does not incorporate the single-photon cross-section that is so significant in the S.P.I. model.

13 Multiple ionization of C_{60}

Let us now turn our attention to C_{60}. The published (multiple) ion yield curves for this molecule [56–58] are in severe conflict with each other. None of the results can be reproduced using the single-photon photoabsorption cross-sections [59,60]. However, the ion yields of Campbell et al. [58] for C_{60}^{+}... C_{60}^{4+} can be reproduced satisfactorily, assuming that the individual carbon atoms behave as independent ionization centers. Let us label the timelets with $k = 1, 2, ..., K$ as before, and write p_k for the S.P.I. ionization probability of a single carbon atom due to timelet k, and n_k^{Q+} for the probability that Q of the 60 carbon atoms in C_{60} are ionized after timelet k. We then calculate the distribution of charge states after the pulse $n_{k=K}^{Q+}$ in an iterative way:

$$n_k^{Q+} = \sum_{q=0}^{Q} \binom{60-Q+q}{q} p_k^q (1-p_k)^{60-Q}\, n_{k-1}^{(Q-q)+}. \quad (17)$$

Equation (17) adds all probabilities to obtain C_{60}^{Q+} from $C_{60}^{(Q-q)+}$ in a process where exactly q of the $60-(Q-q)$ carbon atoms that remained neutral after timelet $k-1$ are ionized due to timelet k. The volume-integrated curves in Figure 9 show that we then find comparable saturation intensities for C_{60}^{+}... C_{60}^{4+}, in agreement with the experimental data from reference [58]. (In Fig. 9 we reduced the experimental intensities by a factor of 1.75.) Equation (17) predicts $C_{60}^{Q+} \propto I^{7Q}$ for very low intensities. However, as explained above, we expect weaker dependences to be observed if this order $7Q$ is large. This is in agreement with the data reported by [58]. Our calculations predict that around the saturation intensity several charge states occur simultaneously with comparable probabilities (e.g. C_{60}^{+}... C_{60}^{5+} all between 11% and 23%), and there is no intensity for which only one charge state dominates (except, of course, for very low intensities, where C_{60}^{+} dominates). Such subtleties are obscured in most experiments, because ions are usually collected from the whole focal region which results in yields ordered as $C_{60}^{+} > C_{60}^{2+} > C_{60}^{3+}$..., each signal having an $I^{3/2}$ dependence [61] due to focal volume expansion (see Fig. 9). Thus, the C_{60} system is an ideal candidate for investigations using a three-dimensionally confined, μm-sized detection volume [62,63]. Overlapping this confined volume with the heart of the focus allows the determination of absolute ionization probabilities [64], thus avoiding the blurring influence of volume expansion and rendering the exact shape of the spatial intensity distribution irrelevant.

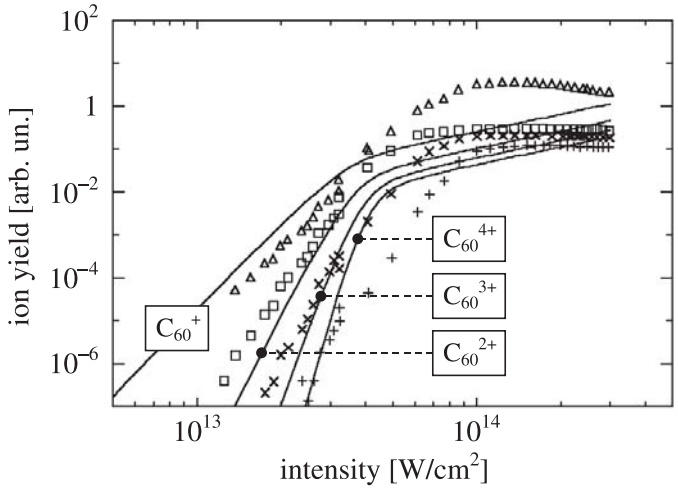

Fig. 9. Ionization behavior of C_{60} upon irradiation with a linearly polarized 25-fs pulse of 790-nm wavelength. Solid curves: present model. Experimental data from reference [58]: $\triangle = C_{60}^{+}$; $\square = C_{60}^{2+}$; $\times = C_{60}^{3+}$; $+ = C_{60}^{4+}$. For an optimal fit, the experimental intensities were reduced by a factor of 1.75.

14 Conclusions

We have investigated intense field ionization with photons of energy $E_{\rm ph}$ on the basis of four heuristic assumptions: (1) Each target particle continuum level E_m with energy $E_m = mE_{\rm ph}$ is a possible doorway state towards ionization; (2) Each of these levels E_m has a characteristic electronic response time $\Delta t_m = h/E_m = T/m$ (timelet), and within this time interval the target particle is unable to alter its state upon the photobombardment; (3) For times shorter than Δt_m the target particle cannot distinguish between the energy delivered by m photons and the energy delivered by a single photon with energy $E_m = mE_{\rm ph}$, so that single-photon cross-sections σ_m for photons with energy $E_m = mE_{\rm ph}$ properly describe the particle's absorption qualities; (4) Ionization (transition to a continuum state with energy $E_m = mE_{\rm ph}$) takes place when the number of photons with energy $E_{\rm ph}$ that passes through the cross-section σ_m within the duration of the timelet h/E_m is equal to or larger than m. For both linear and circular polarization, ion yields and ATI spectra can be closely approximated by a simple analytic expression. Specific properties of a target particle naturally enter into the S.P.I. model through the target particle's characteristic single-photon cross-section. We have shown that the predictions of the S.P.I. model are in accordance with existing experimental evidence. The S.P.I. model successfully describes suppressed ionization, which results from interference of atomic sites in a molecule, a property that is automatically accounted for in single-photon cross-sections. The S.P.I. model gives an alternative explanation of barrier suppression ionization (BSI), and it correctly predicts generalized multiphoton ionization cross-sections for the noble gases. It also properly describes the influence of polarization on the ionization probability. The S.P.I. model explicitly separates the direct photoionization from any other, time-cumulative phenomena such as the ponderomotive potential [39], or electron recollisions [49]. Because such time-cumulative phenomena are probably of lesser importance for few cycle pulses, we expect the S.P.I. model to be well suited to describe photoionization processes with such pulses.

With great pleasure we acknowledge many valuable and encouraging discussions with S.L. Chin. We thank A. Saenz and G.G. Paulus for stimulating comments.

Appendix

To elucidate our S.P.I. model we turn to time-dependent perturbation theory, applying its formalism to a transition from the (unperturbed) ground state $|g\rangle$ to an (unperturbed) ionized state $|z\rangle$.

Let us assume the perturbation $V = -\mu(\mathcal{E}e^{-i\omega t} + \text{c.c.})$ [$\mathcal{E}$ denotes the amplitude of the electric field] is switched on at $t = 0$, and that the number of photons with energy $E_{\rm ph} = \hbar\omega$ needed to reach state z is m. The probability $p_z^{(m)}(t)$ to find the system in state z at time t is then due to an interaction m-th order in the field [65]:

$$p_z^{(m)}(t) = \left| \sum_{p,q,\ldots y} \frac{\overbrace{\mu_{zy}\ldots\mu_{qp}\mu_{pg}}^{m \text{ matrix elements}} \mathcal{E}^m}{\hbar^m \underbrace{(\omega_{yg} - [m-1]\omega)\ldots(\omega_{qg} - 2\omega)(\omega_{pg} - \omega)}_{m-1 \text{ frequencies}}} \times \frac{[e^{i(\omega_{zg} - m\omega)t} - 1]}{(\omega_{zg} - m\omega)} \right|^2 . \quad (18)$$

This expression involves $m - 1$ sums, each running over the complete set of energy eigenstates $|i\rangle$ of the unperturbed system, and we use $\mu_{ij} = \langle i|e\mathbf{r}|j\rangle$ and $\omega_{ij} = (E_i - E_j)/\hbar$.

The S.P.I. model can be shown to result from two drastic simplifications of this expression. Making these simplifications forces us to pass by certain delicacies of equation (18), so that we cannot expect the result to be exact. Nevertheless, our aim is to obtain an expression that is still accurate enough to serve as some sort of guideline to describe intense-field ionization processes. The first simplification is based on the assumption that the frequencies $\omega_{yg}, \ldots, \omega_{qg}, \omega_{pg}$ are all $\approx m\omega$ [66]. A plausibility argument behind this is that for most target particles the bulk of the oscillator strength is found in the continuum, and there is a tendency for the oscillator strength to be largest for energies immediately over the ionization threshold. With this simplification, equation (18) becomes (using completeness,

$\sum_i |i\rangle\langle i| = \hat{I}$):

$$p_z^{(m)}(t) \approx \left| \frac{1}{m!} m\omega \frac{(\overbrace{\mu...\mu\mu}^{m \text{ times}})_{zg} \mathcal{E}^m}{(\hbar\omega)^m} \right|^2 \left| \frac{[e^{i(\omega_{zg} - m\omega)t} - 1]}{(\omega_{zg} - m\omega)} \right|^2 . \quad (19)$$

The second simplification addresses the matrix element

$$(\underbrace{\mu...\mu\mu}_{m \text{ times}})_{zg} = \langle z|\mu...\mu\mu|g\rangle = e^m \int d\mathbf{r}\ \psi_z^\star(\mathbf{r})\, x^m\, \psi_g(\mathbf{r}) \quad (20)$$

(we assume linear polarization in the x-direction; e = elementary charge). This quantity must be on the order of $e^m b^m$, with b being some typical size of the target. To characterize the target in this sense, we chose to take the square root of the single-photon cross-section: $eb \sim \mu_{zg} = e \int d\mathbf{r}\ \psi_z^\star(\mathbf{r})\ x\ \psi_g(\mathbf{r})$, getting

$$(\underbrace{\mu...\mu\mu}_{m \text{ times}})_{zg} \approx (\mu_{zg})^m. \quad (21)$$

An argument in favor of this approximation might be found in the fact that the ground state wave function $\psi_g(\mathbf{r})$ is localized: it extends in a rapidly decreasing fashion into the classically forbidden part of the binding potential of the ionic core. With this in mind, it is interesting to note that the integrand in equation (20) contains the product $x^m \psi_g(\mathbf{r})$. This product is expected to peak somewhere close to the core, having a peak value on the order of b^m.

With these assumptions we arrive at the following estimation for the ionization probability due to half an optical cycle (HC: $t = \frac{1}{2}T = \pi/\omega$):

$$p_z^{(m)}(\text{HC}) \approx \frac{M^m}{m!} \quad (22)$$

with

$$M = \frac{\sigma_m}{E_{\text{ph}}} \Delta t_m I_{\text{peak}} \qquad (I_{\text{peak}} = \varepsilon_0 c \mathcal{E}^2), \quad (23)$$

in which σ_m is the single-photon cross-section connecting states g and z, and $\Delta t_m \equiv T/m$, exactly as in equation (2).

Equation (22) was derived from perturbation theory, an underlying assumption of which is that all excitation probabilities are negligible: nearly all target particles will remain in the ground state, and $M \ll 1$. Obviously, perturbation theory must fail when one deals with intense interactions as is the case in intense-field ionization. Thus, an extension to equation (22) is needed. In the perturbation picture, the transition $g \rightarrow z$ takes place by the simultaneous absorption of m photons. All these photons are energetically needed to excite the target. A natural extension to this picture is obtained when one allows for the involvement of more than this minimum number. The additional photons will then not be used to further excite the ionic core, but rather to give the photoelectron additional kinetic energy (see Sect. 7 on ATI spectra). With all this in mind, we add higher-order terms to the photoionization probability, which then becomes $P_m(\text{HC}) \propto \sum_{s=m}^{\infty} \frac{M^s}{s!}$, or, when properly normalized:

$$P_m(\text{HC}) = e^{-M} \sum_{s=m}^{\infty} \frac{M^s}{s!}. \quad (24)$$

Equation (24) is identical to equation (3). With the normalization we have saturation for high intensities (large M):

$$\lim_{M\to\infty} P_m(\text{HC}) = 1, \quad (25)$$

and the perturbative expression is simply the leading term of equation (24) for very low intensities (small M):

$$P_m(\text{HC}) \approx \frac{M^m}{m!} \quad \text{for } M \ll 1. \quad (26)$$

The above expressions can be reinterpreted in line with Section 2 of this paper: intense field ionization processes can be described using the single photon absorption spectrum in the continuum *and* a statistical analysis of the photon flux on the time scale of the electronic response time of the system under consideration.

References

1. L.V. Keldysh, Zh. Eksp. Teor. Fiz. **47**, 1945 (1964) [English translation: Sov. Phys. JETP **20**, 1307 (1965)]
2. For a recent review see C. J. Joachain, M. Dörr, N. Kylstra, Adv. At. Mol. Opt. Phys. **42**, 225 (2000)
3. A. Becker et al., Phys. Rev. A **64**, 023408 (2001)
4. N.B. Delone, V.P. Krainov, *Multiphoton Processes in Atoms* (Springer, Berlin, 1994)
5. S. Augst et al., J. Opt. Soc. Am. B **8**, 858 (1991)
6. C. Guo, Phys. Rev. Lett. **85**, 2276 (2000)
7. J. Muth-Böhm, A. Becker, F.H.M. Faisal, Phys. Rev. Lett. **85**, 2280 (2000)
8. A. Saenz, J. Phys. B **33**, 4365 (2000)
9. A. Talebpour, J. Yang, S.L. Chin, Opt. Commun. **163**, 29 (1999)
10. C. Guo et al., Phys. Rev. A **58**, R4271 (1998)
11. M.V. Ammosov et al., Adv. At. Mol. Opt. Phys. **29**, 33 (1992)
12. P. Lambropoulos, Comm. At. Mol. Phys. **20**, 199 (1987)
13. P. Lambropoulos, X. Tang, J. Opt. Soc. Am. B **4**, 821 (1987)
14. J. Berkowitz, *Photoabsorption, Photoionization, and Photoelectron Spectroscopy* (Academic, New York, 1979)
15. E.E. Rennie et al., Chem. Phys. **229**, 107 (1998)
16. H.W. Jochims, H. Baumgärtel, S. Leach, Astron. & Astrophys. **314**, 1003 (1996)
17. Y. Iida et al., Chem. Phys. **105**, 211 (1986)
18. G.H. Ho et al., J. Chem. Phys. **109**, 5868 (1998)
19. D.M.P. Holland et al., Chem. Phys. **219**, 91 (1997)
20. G. Cooper et al., Chem. Phys. **125**, 307 (1988)
21. D.M.P. Holland et al., Chem. Phys. **173**, 315 (1993)
22. W.F. Chan et al., Phys. Rev. A **46**, 149 (1992)
23. S. Daviel et al., Chem. Phys. **83**, 391 (1984)
24. D.A. Shaw et al., Chem. Phys. **198**, 381 (1995)

25. W.F. Chan, G. Cooper, C.E. Brion, Chem. Phys. **178**, 401 (1993)
26. W.F. Chan, G. Cooper, C.E. Brion, Chem. Phys. **170**, 123 (1993)
27. C. Backx, G.R. Wight, M.J. Van der Wiel, J. Phys. B **9**, 315 (1976)
28. M. Yan, H.R. Sadeghpour, A. Dalgarno, Astrophys. J. **496**, 1044 (1998)
29. W.F. Chan, G. Cooper, C.E. Brion, Chem. Phys. **168**, 375 (1992)
30. D.A. Shaw et al., Chem. Phys. **166**, 379 (1992)
31. W.F. Chan et al., Chem. Phys. **170**, 81 (1993)
32. W.F. Chan et al., Phys. Rev. A **45**, 1420 (1992)
33. W.F. Chan, G. Cooper, C.E. Brion, Phys. Rev. A **44**, 186 (1991)
34. C.E. Brion, A. Hamnet, Adv. Chem. Phys. **45**, 1 (1981)
35. D.A. Verner et al., Astrophys. J. **465**, 487 (1996)
36. Y. Hatano, Phys. Rep. **313**, 109 (1999)
37. See e.g. D.P. Seccombe et al., J. Chem. Phys. **114**, 4058 (2001)
38. A. Becker, F.H.M. Faisal, Phys. Rev. A **50**, 3256 (1994)
39. M. Protopapas, C.H. Keitel, P.L. Knight, Rep. Prog. Phys. **60**, 389 (1997)
40. G.G. Paulus et al., Nature **414**, 182 (2001)
41. T.D.G. Walsh, J.E. Decker, S.L. Chin, J. Phys. B **26**, L85 (1993)
42. S.M. Hankin et al., Phys. Rev. A **64**, 013405 (2001)
43. D.A.L. Kilcoyne et al., J. Electr. Spectr. Rel. Phen. **36**, 153 (1985)
44. M.J. DeWitt, E. Wells, R.R. Jones, Phys. Rev. Lett. **87**, 153001 (2001)
45. D.A.L. Kilcoyne, S. Nordholm, N.S. Hush, Chem. Phys. **107**, 197 (1986)
46. J.W. Cooper, Phys. Rev. **128**, 681 (1962)
47. B. Witzel et al., Phys. Rev. A **58**, 3836 (1998)
48. G.G. Paulus et al., Phys. Rev. Lett. **72**, 2851 (1994)
49. P.B. Corkum, Phys. Rev. Lett. **71**, 1994 (1993)
50. F. Grasbon et al., Phys. Rev. A **63**, 041402 (2001)
51. S. Augst et al., Phys. Rev. A **52**, R917 (1995)
52. C.J.G.J. Uiterwaal et al., Phys. Rev. A **57**, 392 (1998)
53. S. Augst, D.D. Meyerhofer, Laser Phys. **4**, 1155 (1994)
54. A.M. Müller et al., J. Chem. Phys. **112**, 9289 (2000)
55. D.N. Fittinghoff et al., Phys. Rev. A **49**, 2174 (1994)
56. S. Hunsche et al., Phys. Rev. Lett. **77**, 1966 (1996)
57. M. Tchaplyguine et al., J. Chem. Phys. **112**, 2781 (2000)
58. E.E.B. Campbell et al., J. Chem. Phys. **114**, 1716 (2001)
59. J. Berkowitz, J. Chem. Phys. **111**, 1446 (1999)
60. R. Jaensch, W. Kamke, Mol. Mat. **13**, 143 (2000)
61. S. Speiser, J. Jortner, Chem. Phys. Lett. **44**, 399 (1976)
62. M. Wagner, H. Schröder, Int. J. Mass Spectrom. Ion Proc. **128**, 31 (1993)
63. B. Witzel et al., Int. J. Mass Spectrom. Ion Proc. **172**, 229 (1998)
64. B. Witzel et al., Phys. Rev. A **58**, 3836 (1998) [erratum Phys. Rev. A **59**, 3141 (1999)]
65. R.W. Boyd, *Nonlinear Optics* (Academic, Amsterdam, 2003)
66. A similar assumption is made in reference [12]
67. A. Yokoyama et al., J. Chem. Phys. **92**, 4222 (1990)
68. A. Talebpour, S. Larochelle, S.L. Chin, J. Phys. B **31**, 2769 (1998)
69. Chun He, C.H. Becker, Phys. Rev. A **55**, 1300 (1997)
70. C. Cornaggia, P. Hering, Phys. Rev. A **62**, 023403 (2000)
71. A. Talebpour et al., Chem. Phys. Lett. **313**, 789 (1999)
72. G.R. Burton et al., Chem. Phys. **167**, 349 (1992)
73. Chunlei Guo, Ming Li, G.N. Gibson, Phys. Rev. Lett. **82**, 2492 (1999)
74. D. Charalambidis et al., Phys. Rev. A **50**, R2822 (1994)
75. S.F.J. Larochelle, A. Talebpour, S.L. Chin, J. Phys. B **31**, 1215 (1998)
76. A. Talebpour, C.-Y. Chien, S.L. Chin, J. Phys. B **29**, 5725 (1996)
77. P. Dietrich, P.B. Corkum, J. Chem. Phys. **97**, 3187 (1992)
78. A. Talebpour, Y. Liang, S.L. Chin, J. Phys. B **29**, 3435 (1996)
79. G.N. Gibson et al., Phys. Rev. Lett. **79**, 2022 (1997)
80. A. Talebpour, S. Larochelle, S.L. Chin, J. Phys. B **31**, L49 (1998)
81. A.I. Pegarkov, E. Charron, A. Suzor-Weiner, J. Phys. B **32**, L363 (1999)
82. M.D. Perry et al., Phys. Rev. A **37**, 747 (1988)
83. A. Becker, F.H.M. Faisal, Phys. Rev. A **59**, R1742 (1999)
84. K. Kondo et al., Phys. Rev. A **48**, R2531 (1993)
85. B. Walker et al., Phys. Rev. Lett. **73**, 1227 (1994)